

# GLOBAL SIMULATIONS OF MAGNETOROTATIONAL INSTABILITY IN THE COLLAPSED CORE OF A MASSIVE STAR

H. SAWAI<sup>1</sup>, S. YAMADA<sup>2</sup>, AND H. SUZUKI<sup>1</sup>

*Not to appear in Nonlearned J., 45.*

## ABSTRACT

We performed the first numerical simulations of magnetorotational instability from a sub-magnetar-class seed magnetic field in core collapse supernovae. As a result of axisymmetric ideal MHD simulations, we found that the magnetic field is greatly amplified to magnetar-class strength. In saturation phase, a substantial part of the core is dominated by turbulence, and the magnetic field possesses dominant large scale components, comparable to the size of the proto-neutron star. A pattern of coherent channel flows, which generally appears during exponential growth phase in previous local simulations, is not observed in our global simulations. While the approximate convergence in the exponential growth rate is attained by increasing spatial resolution, that of the saturation magnetic field is not achieved due to still large numerical diffusion. Although the effect of magnetic field on the dynamics is found to be mild, a simulation with a high-enough resolution might result in a larger impact.

*Subject headings:* supernovae: general — magnetohydrodynamics (MHD) — Instabilities — methods: numerical — stars: magnetars

## 1. INTRODUCTION

The explosion mechanism of core-collapse supernovae (CCSNe) is still unresolved despite persistent efforts by many researchers over several decades. Recent state-of-art simulations show that the neutrino heating mechanism assisted by hydrodynamical instabilities revives the accretion shock, i.e., the explosion results in. However, estimated explosion energies are smaller than canonical value of order  $10^{51}$  erg (e.g., Marek & Janka 2009; Suwa et al. 2010).

Meanwhile, effects of magnetic field on the explosion dynamics has been studied well for the decade. Numerical simulations assuming a strong poloidal magnetic field (typically  $10^{12}$ – $10^{13}$  G at the pre-collapse phase), and rapid rotation in most cases, show that magnetic force assists in driving the energetic explosion (e.g., Yamada & Sawai 2004; Obergaulinger et al. 2006; Burrows et al. 2007; Takiwaki et al. 2009; Sawai et al. 2013). The magnetic fields assumed in these simulations are so strong that the conservation of magnetic flux during collapse results in the field strength of  $\gtrsim 10^{15}$  G for the proto-neutron star surface. This is comparable to inferred surface magnetic fields of magnetar candidates (see Woods & Thompson 2006, for review of magnetars).

At present, however, the strength of the magnetic field at the pre-collapse stage and the origin of strong magnetic field of magnetar are very uncertain. Stellar evolution simulations by Heger et al. (2005), which implement Tayler–Spruit dynamo model, show that the pre-collapse strength of the poloidal magnetic field in  $15 M_{\odot}$  star is only  $10^6$  G. Meanwhile, recent observations report that some OB stars in the main sequence stage possess an  $\sim 1$  kG surface magnetic field (e.g., Wade et al. 2012), which corresponds to magnetar-class magnetic flux. Ferrario & Wickramasinghe (2006) car-

ried out a population synthesis calculation from main sequence stars to neutron stars, assuming the magnetic flux is conserved in the post-main-sequence evolution (fossil field hypothesis). Their result implies that  $\sim 10\%$  of OB stars have magnetar-class magnetic flux, while the majority have  $\sim 1$ – $2$  orders of magnitude weaker one.

Even when the pre-collapse magnetic flux is weak, corresponding to the magnetic field of  $\lesssim 10^{13}$  G for the proto-neutron star surface, MHD instabilities may amplify it to magnetar-class strength. So far, there have been a small number of works focusing on this issue. Thompson & Duncan (1993) argued that convective dynamo in proto-neutron stars generates a magnetar-class magnetic field. Simulations performed by Endeve et al. (2012) shows that standing accretion shock instability amplifies the magnetic field around the proto-neutron star surface from  $\sim 10^{12}$  G to  $\sim 10^{14}$  G. For rapidly rotating progenitors, magnetorotational instability (MRI, Balbus & Hawley 1991) may greatly amplify the magnetic field (Akiyama et al. 2003). Local box simulations characterizing a post-bounce core show that an initially weak magnetic field,  $\sim 10^{12}$ – $10^{13}$  G inside the proto-neutron star, exponentially grows due to MRI (Obergaulinger et al. 2009; Masada et al. 2012).<sup>3</sup>

In simulations of MRI from a sub-magnetar-class seed magnetic field,  $\lesssim 10^{13}$  G, a quite fine grid size compared to the scale of the iron core, e.g.,  $\sim 1000$  km, is required: The wavelength of maximum growing mode around the surface of the proto-neutron star is

$$\lambda_{\text{MGM}} \sim \frac{2\pi v_A}{\Omega} \sim 20\text{m} \left( \frac{\rho}{10^{12}\text{g cm}^{-3}} \right)^{-\frac{1}{2}} \left( \frac{B}{10^{12}\text{G}} \right) \left( \frac{\Omega}{10^3\text{rad s}^{-1}} \right)^{-1} \quad (1)$$

<sup>3</sup> In the simulations performed by Obergaulinger et al. (2009), although the size of the simulation box is small,  $\sim 1$  km, compared to the iron core, the global gradients of physical quantities are taken into account, by which they refer these simulations semi-global.

hsawai@rs.tus.ac.jp

<sup>1</sup> Tokyo University of Science, Chiba 278-8510, Japan

<sup>2</sup> Waseda University, Shinjuku, Tokyo 169-8555, Japan

where  $v_A$  is Alfvén velocity. In order to attain such a high resolution, local simulations are adopted in previous works (Obergaullinger et al. 2009; Masada et al. 2012). However, in local simulations, it is problematic to prepare a suitable background state: Although an initially stationary background is usually used in local simulations, post-bounce cores are dynamical. Additionally, local simulations are incapable of studying the global dynamics. To relieve these problems, global simulations are desirable.

In this letter, we report the first global simulations of MRI in CCSNe from a seed magnetic field of sub-magnetar-class flux. To ease high computational cost demanded in global simulations, we carried out computations in axisymmetry and in limited radial range, 50–500 km. Particular attention is paid to, (i) whether MRI amplify the magnetic field to magnetar-class strength even in the dynamical background of CCSNe, and (ii) whether the amplified magnetic field is strong enough to affect the dynamics.

## 2. NUMERICAL METHODS

In the simulations, we solve the following ideal MHD equations, employing a time-explicit Eulerian MHD code, *Yamazakura* (Sawai et al. 2013):

$$\frac{\partial \rho}{\partial t} + \nabla \cdot (\rho \mathbf{v}) = 0, \quad (2)$$

$$\begin{aligned} \frac{\partial}{\partial t} (\rho \mathbf{v}) + \nabla \cdot \left( \rho \mathbf{v} \mathbf{v} - \frac{\mathbf{B}\mathbf{B}}{4\pi} \right) \\ = -\nabla \left( p + \frac{B^2}{8\pi} \right) - \rho \nabla \Phi, \end{aligned} \quad (3)$$

$$\begin{aligned} \frac{\partial}{\partial t} \left( e + \frac{\rho v^2}{2} + \frac{B^2}{8\pi} \right) \\ + \nabla \cdot \left[ \left( e + p + \frac{\rho v^2}{2} + \frac{B^2}{4\pi} \right) \mathbf{v} \right. \\ \left. - \frac{(\mathbf{v} \cdot \mathbf{B})\mathbf{B}}{4\pi} \right] = -\rho (\nabla \Phi) \cdot \mathbf{v}, \end{aligned} \quad (4)$$

$$\frac{\partial \mathbf{B}}{\partial t} = \nabla \times (\mathbf{v} \times \mathbf{B}), \quad (5)$$

in which notations of the physical variables follow custom. Here,  $\Phi$  is Newtonian mono-pole gravitational potential. Computations are done with polar coordinates in two dimension, assuming axisymmetry and equatorial symmetry. We adopt a tabulated nuclear equation of state produced by Shen et al. (1998a,b). Neutrinos are not dealt with in our simulations. The electron fraction, which is required to obtain the pressure of a fluid element from the EOS table, is given by a prescription suggested by Liebendörfer (2005). We should note that the Liebendörfer’s prescription is only valid until bounce. Sawai et al. (2013) discussed that adopting this prescription in the post-bounce phase may lead to underestimation of pressure by upto 20%.

Before simulating MRI, we first follow the collapse of a  $15 M_\odot$  progenitor star (S. E. Woosley 1995, private communication) for the central region of 4000 km radius, until  $\sim 100$  ms after bounce (basic run). After the central density reaches  $10^{12}$  g cm $^{-3}$ , the core is covered with  $N_r \times N_\theta = 720 \times 30$  numerical grids, where the spa-

tial resolution is 0.4–23 km. The core is assumed to be rapidly rotating with the initial angular velocity profile of

$$\Omega(r) = \Omega_0 \frac{r_0^2}{r_0^2 + r^2}, \quad (6)$$

where  $r_0 = 1000$  km and  $\Omega_0 = 3.9$  rad s $^{-1}$ , corresponding to a millisecond proto-neutron star after collapse. The same dipole-like magnetic field configuration as one employed by Sawai et al. (2013) is initially assumed with the typical field strength of  $\sim 10^{11}$  G around the pole inside a radius of 1000 km, with which the strength of  $\sim 10^{13}$  G is obtained for the proto-neutron star surface. The initial rotational energy and magnetic energy divided by the gravitational binding energy are  $5.0 \times 10^{-3}$  and  $5.3 \times 10^{-7}$ , respectively.

To conduct high resolution global simulations to capture the growth of MRI in the core, we restrict the numerical domain to a radial range of  $50 < (r/\text{km}) < 500$  (MRI run). The initial condition of MRI run is set by mapping the data of basic run onto the above domain, at 5 ms after bounce. At that time, the density at the inner-most grids is  $(1.5\text{--}2.2) \times 10^{11}$  g cm $^{-3}$ . The inner and outer radial boundary conditions for MRI run are given by the data of basic run, except for  $B_r$ . The boundary values of  $B_r$  are given so that the divergence free condition of the magnetic field is satisfied. The grid spacing is such that the radial and angular grid sizes are same, viz.  $\Delta r = r \Delta \theta$ , at the inner and outer most cells. We perform MRI runs with four different grid resolutions, where the grid sizes of the inner most cells,  $\Delta r_{\min}$ , (and the numbers of grids,  $N_r \times N_\theta$ ) are 12.5 m ( $8900 \times 6400$ ), 25 m ( $4700 \times 3200$ ), 50 m ( $2300 \times 1600$ ), and 100 m ( $1200 \times 800$ ). Note that with above parameters, typical MRI growth wavelength around the inner boundary is several 100 m at the beginning of MRI runs. We stop each MRI run, before the shock surface reaches the outer boundary.

## 3. RESULTS

In each MRI run, we found a clear exponential growth of the poloidal magnetic energy during  $t \approx 4\text{--}18$  ms, where  $t = 0$  ms corresponds to the beginning of MRI run (see left panel of Figure 1). The growth timescale is larger for higher grid resolution, but almost converges to  $\tau_{\text{MRI,num}} \approx 8$  ms at MRI run with  $\Delta r_{\min} = 25$  m. Afterward, the poloidal magnetic energy gradually increases, and roughly saturates around  $t \approx 50$  ms, in which the saturation energy is larger for higher grid resolution. The evolution of toroidal magnetic energy does not show clear exponential growth in each MRI run. Although the growth rate is initially larger compared with that of the poloidal magnetic energy, it becomes smaller after the exponential growth of the poloidal magnetic energy sets in. At saturation, in MRI run with  $\Delta r_{\min} = 12.5$  m, the poloidal magnetic energy is twice as large as the toroidal magnetic energy.

We also follow the variation of the poloidal magnetic field structure, for MRI run with  $\Delta r_{\min} = 12.5$  m. Around  $t \approx 4$  ms, when the exponential growth begins, magnetic field lines around the pole in the vicinity of the inner boundary start to bend. During the exponential growth phase, the magnetic field lines in this region

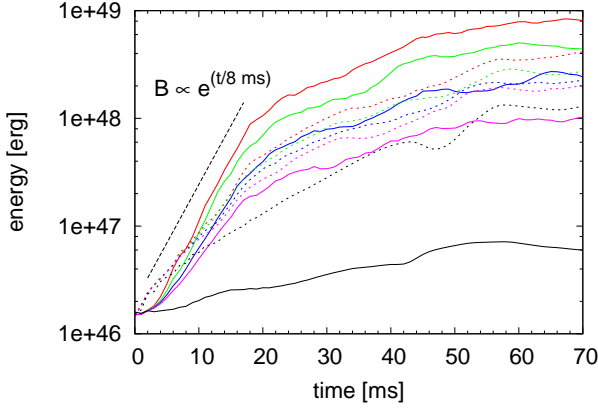


**Figure 1.** Evolutions of the poloidal magnetic energies (solid lines) and the toroidal magnetic energies (dotted lines) for MRI run with  $\Delta r_{\min} = 12.5$  m (red lines),  $\Delta r_{\min} = 25$  m (green lines),  $\Delta r_{\min} = 50$  m (blue lines),  $\Delta r_{\min} = 100$  m (magenta lines), and basic run (black lines).

are further stretched, and filaments of strong magnetic field,  $\sim 10^{14}$  G, appear (see panel (a) of Figure 2 for  $t = 11$  ms). After the exponential growth ceases, the topology of magnetic field lines becomes rather tangled, which implies that the flow becomes turbulent (see panel (b) for  $t = 20$  ms). Subsequently, filaments of strong magnetic field and the turbulent flow pattern, which first appear around the pole, also emerge in other regions. This phase corresponds to the duration of the gradual increase of the poloidal magnetic energy,  $t \approx 18$ –50 ms, observed in Figure 1. After the poloidal magnetic energy saturates ( $t \approx 50$  ms), a considerable fraction inside a radius of 150 km is dominated by turbulent flow, where the strength of the magnetic field reaches  $\sim 10^{14}$ – $10^{15}$  G in filamentous flux tubes (see panel (c) for  $t = 70$  ms).

The bent magnetic field lines, the exponential growth of the poloidal magnetic field, the fact the growth rate is larger for higher grid resolution, and the turbulence after the exponential growth, all invoke the occurrence of MRI in our simulations. As seen in panel (e) of Figure 2, the number of grids covering the maximum growing wavelength in MRI run with  $\Delta r_{\min} = 12.5$  m is more than 20 in most areas, although it is less than five in some limited locations in the vicinity of the pole and equator. Thus, our highest-resolution MRI run seems almost capable to fairly capture the linear growth of MRI. According to Akiyama et al. (2003), the growth timescale obtained by the linear theory is

$$\tau_{\text{MRI,th}} = 2\pi \left| (\eta^2 - 2\eta + 1)\Omega^2 + \frac{\eta - 1}{2} \left( \xi N^2 + \eta \frac{d\Omega^2}{d \ln r} \right) + \frac{1}{16\Omega^2} \left( \xi N^2 + \eta \frac{d\Omega^2}{d \ln r} \right)^2 \right|^{-1/2}, \quad (7)$$

where

$$\xi^2 = (1 - \sin 2\theta)^2, \quad (8)$$

$$\eta^2 = \sin^2 \theta (1 - \sin 2\theta). \quad (9)$$

In panel (f) of Figure 2, the distribution of  $\tau_{\text{MRI,th}}$  for MRI run with  $\Delta r_{\min} = 12.5$  m at 4 ms is depicted. It is found that, except for the very vicinity of the pole, where the grid resolution is not enough, the growth timescale is shortest,  $\tau_{\text{MRI,th}} \sim 10$  ms, around the pole in the vicinity

of the inner boundary. This is consistent with the fact that magnetic field amplification first occurs there. Additionally, the numerically estimated growth timescale,  $\tau_{\text{MRI,num}} \approx 8$  ms (Figure 1), approximately coincides with the above theoretical value. We also estimated  $\tau_{\text{MRI,th}}$  without the effect of the gradient of entropy and the lepton fraction, by setting  $N = 0$  in Equation (7), but found insignificant difference from the original one, which indicates that convection does not much contribute to amplify the magnetic field. With all the above facts, we conclude that amplification of poloidal magnetic field found in our simulations is mainly due to MRI.

Since axisymmetry is assumed in our simulations, the toroidal component of the magnetic field is not directly amplified by MRI. The growth of the toroidal magnetic energy, which is slower than that of the poloidal magnetic energy, seems due to winding of magnetic field lines by differential rotation.

In local simulations performed by Obergaulinger et al. (2009), the pattern of coherent channel flows appears during the exponential growth phase. In our simulations, on the other hand, such a pattern is never observed. Although channel-like configurations are locally observed in the exponential growth phase (see panel (d) of Figure 2), they are incoherent, and soon disrupted in timescale of milliseconds. Such immediate disruption of channel flows seems to be caused by dynamical flow motions in the background, which is difficult to be taken into account in local simulations.

In left panel of Figure 3, the energy spectra of the poloidal magnetic energy are plotted for MRI run with  $\Delta r_{\min} = 12.5$  m at different evolutionary phases. Each spectrum is derived for radial wave numbers,  $k_r$ , and for a region  $50 < (r/\text{km}) < 100$  and  $15^\circ < \theta < 60^\circ$ . At  $t = 4$  ms, the spectrum shows the dominance of a large scale,  $\gtrsim 50$  km, just reflecting the structure of the background magnetic field. During the linear growth phase,  $t \approx 4$ –18 ms, smaller scale structures,  $\lesssim 10$  km, grow fast compared with the larger ones. Consistently, we found that the maximum growing wavelength of MRI around the pole is generally  $\sim 0.1$ –10 km during this phase. At the end of the simulation (saturation phase), the spectrum shows almost flat distribution for  $r \gtrsim 5$  km, and steep decay for  $r \lesssim 1$  km. In the range between them, a slope close to  $\propto k^{-5/3}$  is observed, which seems to correspond to the inertial region of Kolmogorov's theory. Such spectrum affirms that the flow is turbulent. Also, it indicates that large scale components of the magnetic field, comparable to the size of the proto-neutron star, are produced in our simulations. Since the maximum growing wavelength of MRI is generally smaller than this scale, as mentioned above, the large scale components are likely to be a result of inverse cascade.

We also compare the average spectra of the poloidal magnetic energy for  $t = 65$ –70 ms among MRI runs (right panel of Fig 3). It is found that in a lower resolution run, the spectrum tends to turn the steep decay at larger scale, which seems to be due to a larger numerical diffusion. It is likely that this causes smaller spectral energy for a low resolution run over whole scales, and smaller saturation level observed in Figure 1.

Figure 4 shows that magnetic pressure reaches  $\gtrsim 10\%$  of matter pressure in some locations, which implies that

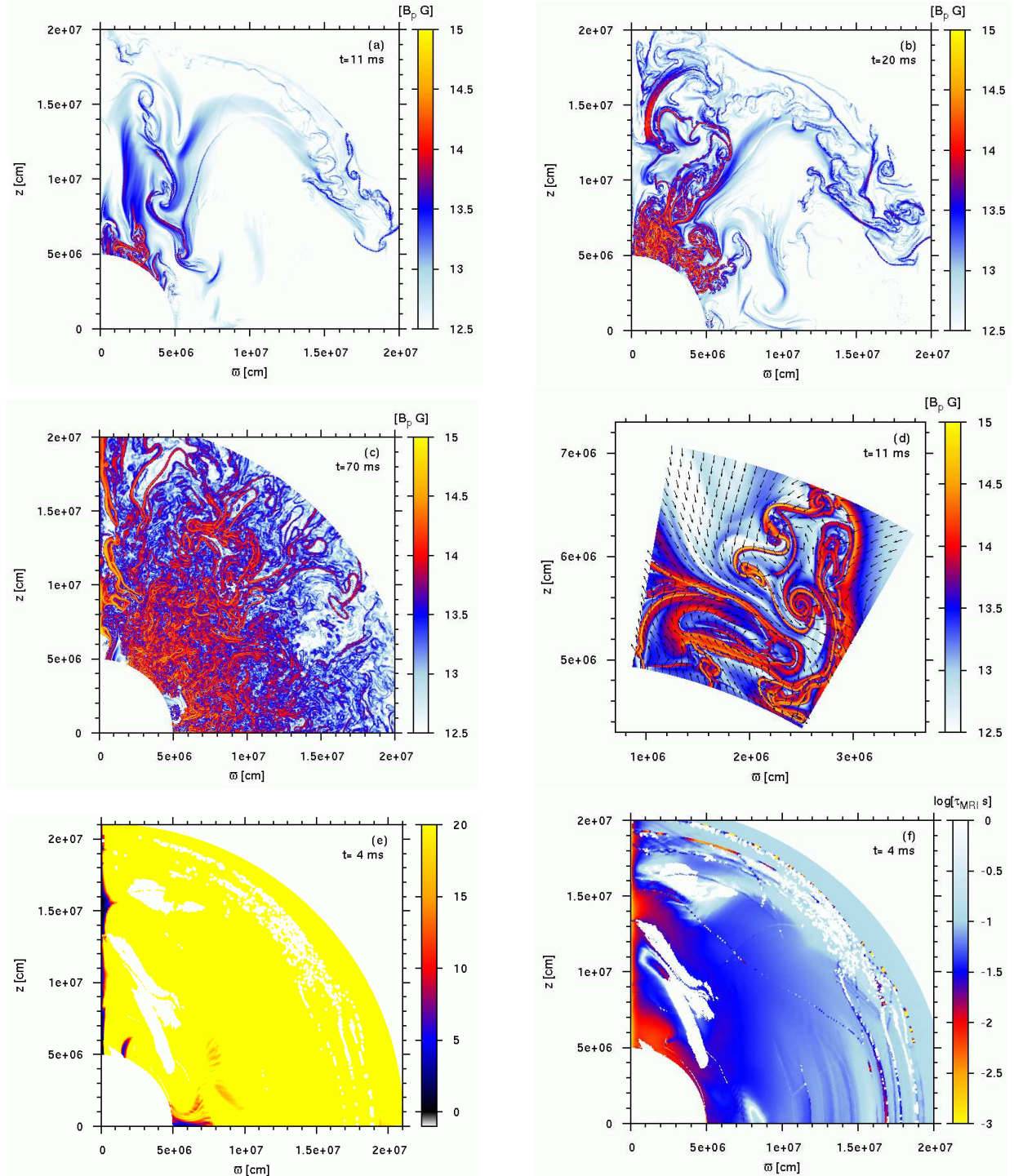


**Figure 2.** (a)–(c): Distribution of poloidal magnetic field strength at (a)  $t = 11$  ms, (b)  $t = 20$  ms, and (c)  $t = 70$  ms. Only a part of the numerical domain is depicted in each panel. (d): Distribution of poloidal magnetic field strength (color) together with velocity directions (arrows) at 11 ms for  $50 \lesssim (r/km) \lesssim 70$  and  $10^\circ \lesssim \theta \lesssim 30^\circ$ . (e): Distribution of the maximum growing wavelength of MRI divided by the grid scale at  $t = 4$  ms. (f): Distribution of the maximum growing timescale of MRI (Equation 7) at  $t = 4$  ms. In panel (e) and (f), white-colored areas include the location stable to MRI. All panels are depicted for MRI run with  $\Delta r_{\min} = 12.5$  m.

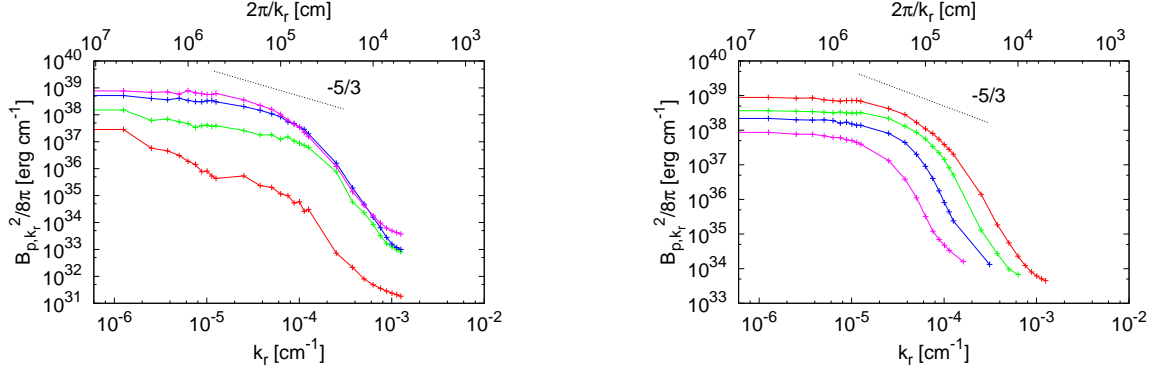


**Figure 3.** Left: Spectra of the poloidal magnetic energy for MRI run with  $\Delta r_{\min} = 12.5$  m at  $t = 4$  ms (red line),  $t = 11$  ms (green line),  $t = 20$  ms (blue line), and  $t = 70$  ms (magenta line). Right: Average spectra of the poloidal magnetic energy over  $t = 65\text{--}70$  ms, for MRI run with  $\Delta r_{\min} = 12.5$  m (red line),  $\Delta r_{\min} = 25$  m (green line),  $\Delta r_{\min} = 50$  m (blue line), and  $\Delta r_{\min} = 100$  m (magenta line). Each spectrum is derived for radial wave numbers,  $k_r$ , and for a region  $50 < (r/\text{km}) < 100$  and  $15^\circ < \theta < 60^\circ$ .

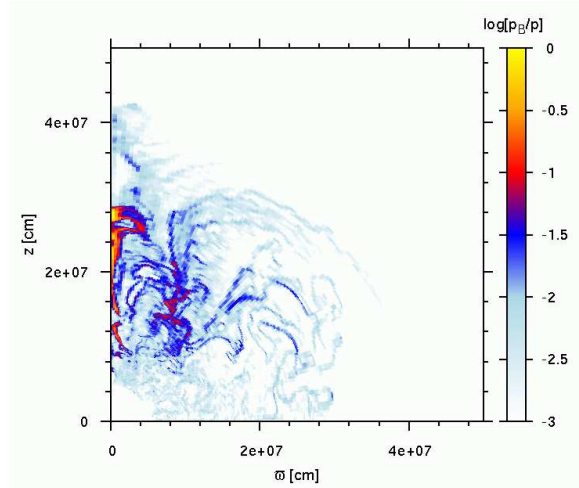


**Figure 4.** Distribution of the ratio of magnetic pressure to matter pressure for MRI run with  $\Delta r_{\min} = 12.5$  m at  $t = 70$  ms.

the magnetic field mildly affects the dynamics. Note, however, that we did not obtain the convergence of the saturation magnetic field, and a larger saturation level is attained for a higher resolution run (Figure 1). This suggests that the simulation with a high-enough resolution might result in a larger impact of the magnetic field on the dynamics.

#### 4. DISCUSSION AND CONCLUSION

We have carried out the first global simulations of MRI in CCSNe from a sub-magnetar-class seed magnetic field,  $\sim 10^{13}$  G around the surface of the proto-neutron star, and rapid rotation, in which two-dimensional ideal MHD equations are solved with assumptions of axisymmetry and equatorial symmetry. As a result of computations, we found that MRI greatly amplifies the magnetic field to magnetar-class strength,  $\sim 10^{14}$ – $10^{15}$  G, and that the magnetic field at saturation phase is dominated by large scale structure. Although, the impact of the magnetic field on the dynamics found to be mild, we do not obtain the convergence of the saturation magnetic field strength, which is larger for a higher resolution run. A simulation with a higher resolution is necessary to assess the actual impact. We also found that the evolution of flow pattern in our global simulations are quite different from those appear in local simulations by Obergaulinger et al. (2009).

Since MRI and turbulence are intrinsically non-axisymmetric phenomena, three-dimensional simulations are, in fact, necessary to lead to conclusive results. Note, however, that even the world's best computers may only be capable to simulate global MRI from a magnetar-class seed magnetic field in three dimension. Obergaulinger et al. (2009) found that the main difference between two-dimensional and three dimensional simulations is that the former results in a larger saturation magnetic field compared with the latter. They argued that the smaller saturation level in three dimension is caused by the disruption of coherent channel flows before they grow well due to non-axisymmetric parasitic instabilities. Such difference might not appear in global simulations, since our simulations show that coherent channel flows do not develop even in two dimension.

While the present simulations set the position of the inner boundary at  $r = 50$  km, we found in basic run that most rotational energy is reserved inside a radius of 50 km. It is expected that a simulation with the inner boundary located at a smaller radius would result in a larger saturation magnetic field. What we obtained in this study may be a lower limit.

Although, in our simulations, a sub-magnetar-class magnetic field is amplified to magnetar-class strength due to MRI, we should be cautious in concluding that MRI can be the origin of magnetar fields. Before that, further investigations may be required on the sustainability of a large scale, strong magnetic field until, e.g.,

the formation of the neutron star. Additionally, it is worth investigating whether magnetar-class strength is also attained by MRI from a weaker seed magnetic field, e.g.,  $< 10^{12}$  G around the proto-neutron star surface. Note that previous local simulations of MRI, including ones in the context of accretion disks, show that a weaker seed magnetic field results in a lower saturation level (e.g., Obergaulinger et al. 2009; Okuzumi & Hirose 2011). The dependence of the saturation magnetic field on the rotational velocity, which also has been discussed in many local simulations (e.g., Masada et al. 2012), is another issue to be studied in future works.

H.S. is grateful to Kenta Kiuchi for useful advice on MPI parallelization. Numerical computations in this work were carried out at the Yukawa Institute Computer Facility. This work is supported by a Grant-in-Aid for Scientific Research from the Ministry of Education, Culture, Sports, Science and Technology, Japan (20105004, 21840050, 24244036.)

#### REFERENCES

- Akiyama, S., Wheeler, J. C., Meier, D. L., & Lichtenstadt, I. 2003, *ApJ*, 584, 954  
 Balbus, S. A. 1995, *ApJ*, 453, 380  
 Balbus, S. A., & Hawley, J. F. 1991, *ApJ*, 376, 214  
 Burrows, A., Dessart, L., Livne, E., Ott, C. D., & Murphy, J. 2007, *ApJ*, 664, 416  
 Endeve, E., Cardall, C. Y., Budiardja, R. D., et al. 2012, *ApJ*, 751, 26  
 Ferrario, L. & Wickramasinghe, D. T. 2006, *Mon. Not. Astron. Soc.*, 367, 1323  
 Heger, A., Woosley, S. E., & Spruit, H. C. 2005, *ApJ*, 626, 350  
 Kitiashvili, I. N., Abramenko, V. I., Goode, P. R., et al. 2012, *arXiv:1206.5300*  
 Liebendörfer, M. 2005, *ApJ*, 633, 1042  
 Marek, A., & Janka, H.-T. 2009, *ApJ*, 694, 664  
 Masada, Y., Takiwaki, T., Kotake, K., & Sano, T. 2012, *ApJ*, 759, 110  
 Obergaulinger, M., Aloy, M. A., & Müller, E. 2006, *A&A*, 450, 1107  
 Obergaulinger, M., Cerdá-Durán, P., Müller, E., & Aloy, M. A. 2009, *A&A*, 498, 241  
 Obergaulinger, M., & Janka, H.-T. 2011, *arXiv:1101.1198*  
 Okuzumi, S., & Hirose, S. 2011, *ApJ*, 742, 65  
 Shen, H., Toki, H., Oyamatsu, K., & Sumiyoshi, K. 1998a, *Nuclear Physics A*, 637, 435  
 Shen, H., Toki, H., Oyamatsu, K., & Sumiyoshi, K. 1998b, *Progress of Theoretical Physics*, 100, 1013  
 Sawai, H., Yamada, S., Kotake, K., & Suzuki, H. 2008, *ApJ* in press  
 Suwa, Y., Kotake, K., Takiwaki, T., et al. 2010, *PASJ*, 62, L49  
 Yamada, S., & Sawai, H. 2004, *ApJ*, 608, 907  
 Takiwaki, T., Kotake, K., & Sato, K. 2009, *ApJ*, 691, 1360  
 Thompson, C., & Duncan, R. C. 1993, *ApJ*, 408, 194  
 Wade, G. A., Grunhut, J., Gräfener, G., et al. 2012, *MNRAS*, 419, 2459  
 Woods, P. M., & Thompson, C. 2006, *Compact stellar X-ray sources*, 547